Code Development on Parallel Partitioned Fluid-Structure Interaction Simulations

Turbulence Vortex-Induced Vibrations of a Blunt Trailing Edge Hydrofoil

Project Report

STFC Hartree Centre
IBM Research UK

Title:
Code Development on Parallel Partitioned Fluid-Structure Interaction Simulations

Theme:
Multi-physical modelling

Participant(s):
Wendi Liu (STFC)*
Wei Wang (STFC)
Alex Skillen (STFC)
Eduardo Ramos Fernandez (IBM)
Stephen Longshaw (STFC)
Robert Sawko (IBM)

Further Information:
If you would like further information about this report or to discuss its content, please contact:
*wendi.liu@stfc.ac.uk

Date of Completion:
June 9, 2020

STFC Hartree Centre
https://www.hartree.stfc.ac.uk
IBM Research UK
http://research.ibm.com/labs/uk/

This work was supported by the STFC Hartree Centre's Innovation Return on Research programme, funded by the Department for Business, Energy & Industrial Strategy.

Contents

1 Introduction **4**

2 Solvers and Governing Equations **6**
2.1 Fluid solver 6
2.2 Structure solver 7
2.3 Fluid structure interaction 8

3 Validation of Framework **14**
3.1 1D Heat Transfer 14
3.2 Beam with Tip Load 15
3.3 2D Flow Pass Rigid Plate Behind a Rigid Cylinder 15
3.4 2D Flow Pass Elastic Plate Behind a Rigid Cylinder 20
3.5 3D Parabolic Flow Over a Firmer Elastic Beam 20
3.6 3D Parabolic Flow Over a Softer Elastic Beam 22

4 Scalability Test of Framework **26**

5 Hydrofoil Case **28**
5.1 Physical properties 28
5.2 Simulation setup 28
5.3 Results on frequency and amplitude of hydrofoil vibration 30
5.4 Instantaneous results on vibration velocity and spectra 30
5.5 Contours on fluid and structure domains 33

6 Conclusions and recommendations **40**

Bibliography **41**

A Partitioned Fluid-Structure Interaction Simulation Framework **42**

Executive Summary

Fluid-Structure Interaction (FSI) is a phenomenon that appears in a wide range of scientific and engineering disciplines at different scales. Due to the non-linear, time-dependent and multi-physical nature of various FSI problems, numerical simulation has a distinct advantage over other investigation methods. There are many in-house/commercial FSI solvers, but few of them can achieve both numerical robustness and high scalability. To develop an effective and robust method for FSI, we choose the partitioned approach to make good use of the existing open-source codes to allow good flexibility and to reduce the effort of maintenance of this framework. For a partitioned approach, a stable and accurate coupling algorithm with good scalability is required. Therefore, the Multi-scale Universal Interface (MUI) coupling library is employed as the interface coupling tool between fluid and structure domains. The MUI library shows good scalability and allows an arbitrary number of codes to communicate with one another over MPI via a cloud of point data. In the present study, the two solvers OpenFOAM and FEniCS are adopted as the computational fluid dynamics (CFD) and computational structure mechanics (CSM) solvers, respectively. Two explicit/implicit coupling utilities for the FSI coupling have been developed in the MUI library to achieve a tight and stable coupling. In order to show the performance of this approach, the simulation of a blunt trailing edge hydrofoil with vortex-shedding induced vibration will be presented. The NACA0009 deformable hydrofoil, operated at zero angle of attack, is modelled at different thick-based Reynolds numbers in the range of 3.8×10^4 - 7.1×10^4 to present the lock-in and the lock-off regimes of the vortex-induced vibration. A comparison between the numerical simulation and the experimental data is carried out. Detailed characteristics of the body oscillation and vortex shedding are also provided.

Technical Report

Chapter 1

Introduction

Fluid-Structure Interaction (FSI) is broadly defined as the study of the interactions between fluid flows and solid structures. It has been applied in a wide range of scientific and engineering disciplines in different scales, such as the hydroelasticity of a hydrofoil, aeroelasticity of industrial steam turbine blades and biomedical FSI of blood flow in a blood vessel. Because of its importance, there is a need to develop an efficient full-order modelling technique to simulate these industrial/scientific challenges on FSI phenomenon, i.e. to produce a digital twin of the experiments for industrial designs. Different types of application of FSI require different functions and treatments. It is better to have a simulation tool that can cope with most cases, or can switch among them quite easily. The simulation tool needs to have a high scalability to simulate such complex geometries with high-fidelity. In addition, robustness and stability are also required for these strong FSI couplings.

The numerical procedures to solve FSI problems can be broadly classified into two approaches: the monolithic approach and the partitioned approach. The monolithic approach treats the fluid and structure dynamics in the same mathematical framework to form a single system equation for the entire problem, which is solved simultaneously by a unified algorithm. The interfacial conditions are implicit in the solution procedure. This approach can potentially achieve stable and accelerated convergence for strong interactions, but it may require more resources and expertise to develop and maintain such a specialized code, and it struggles to cope with different types of FSI applications. The partitioned approach treats the fluid and the structure as two computational fields which can be solved separately with their respective mesh discretisation and numerical algorithm. The interfacial conditions are used explicitly to communicate information between the fluid and structure solutions. A partitioned approach to multi-physics coupling has advantages over a monolithic coupling, since we can make use of many existing codes to boost the code development and maintenance. In addition, a partitioned approach allows coupling of solvers with different discretisations with relative ease, but it is

quite challenging to develop an efficient interface between domains with a good robustness and scalability.

To answer the needs of the industrial challenges, this project intends to develop an effective and robust methodology for FSI simulations with a good scalability. We use the partitioned approach to allow flexibility and extendibility of the framework; it's robustness and scalability are the main focus of this project. An initial test-case has been done comprises an elastic hydrofoil in both intermediate-speed and high-speed flow conditions. The function of this simulation tool will be further extended in the future phases.

The report is organised as follows. The solvers and governing equations are presented in Chapter 2. In Chapter 3, the details of validations of the present FSI framework are described, followed by the results of the preliminary scalability test in Chapter 4. Chapter 5 gives the simulation details and results of the hydrofoil case. Finally, we draw some conclusions and brief overview of the FSI framework in Chapter 6 and Appendix A, respectively.

Chapter 2

Solvers and Governing Equations

2.1 Fluid solver

OpenFOAM is adopted as the fluid solver based on the Computational Fluid Dynamics (CFD) formulations with finite volume discretisation.

In the present framework, the fluid solver is incompressible as the test cases are all based on water with low Mach numbers. The continuity equation reads as [11]:

$$\oint_S \boldsymbol{n} \cdot \boldsymbol{U}\, dS = 0 \tag{2.1}$$

where S is the closed surface of an arbitrary volume V, $\boldsymbol{n}$ is the unit normal pointing outward, $\boldsymbol{U}$ is the fluid velocity. The momentum equation of a general fluid property ϕ over an arbitrary moving volume, which due to the structure deformation, is stated as[3, 11]:

$$\frac{d}{dt}\int_V \rho_f \phi\, dV + \oint_S \rho_f \boldsymbol{n} \cdot (\boldsymbol{U} - \boldsymbol{U_s})\phi\, dS = \oint_S \rho_f \boldsymbol{n} \cdot (\nu_f \nabla \phi)\, dS - \int_V \boldsymbol{s_\phi}\, dV \tag{2.2}$$

where t is the time, ρ_f is the fluid density, $\boldsymbol{U_s}$ is the velocity of the surface S (i.e. the grid velocity), ν_f is the kinematic viscosity of the fluid, and $\boldsymbol{s_\phi}$ is the volume source or sink of ϕ. The formulation of Arbitrary Lagrangian Eulerian (ALE) that described the relation between the rate of change of V and the grid velocity $\boldsymbol{U_s}$ is defined as:

$$\frac{d}{dt}\int_V dV - \oint_S \boldsymbol{n} \cdot \boldsymbol{U_s}\, dS = 0 \tag{2.3}$$

The in-house solver `pimpleFSIFoam` is developed based on the built-in solver `pimpleFoam`. It has the same core algorithms as `pimpleFoam` for the solving of the fluid domain. Additional functions of the `pimpleFSIFoam` compared with the `pimpleFoam` are:

- to calculate the fluid forces in each cell that is located in the interface between the fluid and structure domains and send the forces to the structure solver

- to receive the displacement of each cell that is located in the interface between the fluid and structure domains and move the grid accordingly.
- to conduct sub-iterations for fluid-structure interaction at each time step.

The details will be shown in Section 2.3.

2.2 Structure solver

The in-house structure solver is developed with the libraries of FEniCS based on the Computational Structural Mechanics (CSM) with finite element discretisation. The elastodynamics formulation with the balance of linear momentum is written as:

$$\rho_s \frac{\partial^2 \boldsymbol{d}}{\partial t^2} = \nabla \cdot (J \sigma_s \boldsymbol{F}^{-T}) + \rho_s \boldsymbol{f_s} \tag{2.4}$$

where ρ_s is the density of the structure, $\boldsymbol{d}$ is the structural displacement and $\boldsymbol{f_s}$ expresses the exterior body forces acting on the structure. The deformation gradient $\boldsymbol{F}$ is calculated with the Identity matrix $\boldsymbol{I}$ as:

$$\boldsymbol{F} = \boldsymbol{I} + \nabla \boldsymbol{d} \tag{2.5}$$

and J is the determinant of $\boldsymbol{F}$. In the present solver, the stress tensor σ_s is expressed into two forms. The first form is expressed by Hooke's Law (HL) as:

$$\sigma_s = \frac{1}{J} \boldsymbol{F} (\lambda_s \mathrm{Tr}(\epsilon) \boldsymbol{I} + 2\mu_s \epsilon) \boldsymbol{F}^T \tag{2.6}$$

where $\mathrm{Tr}(A)$ represents the trace of matrix A. The Lamés coefficients λ_s and μ_s are determined by the Poisson's ratio ν_s and the Young's modulus E of the structure as:

$$\lambda_s = \frac{\nu_s E}{(1+\nu_s)(1-2\nu_s)} \tag{2.7}$$

$$\mu_s = \frac{E}{2(1+\nu_s)} \tag{2.8}$$

The strain tensor ϵ is expressed as:

$$\epsilon = \frac{1}{2} (\nabla \boldsymbol{d} + (\nabla \boldsymbol{d})^T) \tag{2.9}$$

The second form of σ_s is expressed by hyper-elastic St. Vernant-Kirchhoff model (STVK) as:

$$\sigma_s = \frac{1}{J} \boldsymbol{F} (\lambda_s Tr(\boldsymbol{G}) \boldsymbol{I} + 2\mu_s \boldsymbol{G}) \boldsymbol{F}^T \tag{2.10}$$

where $\boldsymbol{G}$ is the Green Lagrangian strain tensor that is determined by:

$$\boldsymbol{G} = \frac{1}{2}(\boldsymbol{C} - \boldsymbol{I}) \tag{2.11}$$

The right Cauchy-Green strain tensor $\boldsymbol{C}$ is calculated as:

$$\boldsymbol{C} = \boldsymbol{F}\boldsymbol{F}^{-T} \tag{2.12}$$

HL is limited to small deformations of the structure, while the STVK is able to handle large deformations but valid for small strains [1, 7]. The one-step θ scheme is used for time-stepping of HL and STVK. It can switch among the second-order Crank-Nicholson scheme, the first-order backward-Euler scheme and the first-order forward-Euler scheme by setting the variable as 0.5, 1, and 0, respectively.

The elastodynamics formulation can also be expressed in the form of a generalized n-dof harmonic oscillator (GHO) equation as:

$$\boldsymbol{M}\frac{\partial^2 \boldsymbol{d}}{\partial t^2} + \boldsymbol{K}\boldsymbol{d} = \boldsymbol{F}(t) \tag{2.13}$$

where $\boldsymbol{M}$ is the mass matrix, $\boldsymbol{K}$ is the stiffness matrix and $\boldsymbol{F}$ is the external loads. The dissipation of the structure can be modelled by involving a damping term to 2.13 as:

$$\boldsymbol{M}\frac{\partial^2 \boldsymbol{d}}{\partial t^2} + \boldsymbol{C}\frac{\partial \boldsymbol{d}}{\partial t} + \boldsymbol{K}\boldsymbol{d} = \boldsymbol{F}(t) \tag{2.14}$$

where $\boldsymbol{C}$ is the damping matrix. In the present in-house structure solver, the damping matrix is modelled based on the Rayleigh damping as:

$$\boldsymbol{C} = \alpha_M \boldsymbol{M} + \alpha_k \boldsymbol{K} \tag{2.15}$$

where α_M and α_k are Rayleigh damping parameters. Combining 2.14 and 2.15 gives:

$$\boldsymbol{M}\frac{\partial^2 \boldsymbol{d}}{\partial t^2} + (\alpha_M \boldsymbol{M} + \alpha_k \boldsymbol{K})\frac{\partial \boldsymbol{d}}{\partial t} + \boldsymbol{K}\boldsymbol{d} = \boldsymbol{F}(t) \tag{2.16}$$

The generalized-α method, which is an extension of the Newmark-β method is used to achieve a second order accuracy for the time stepping [4, 2]. The GHO is valid for small deformations of the structure. With the same degree of freedoms (Dof) of the structure domain, the calculation using GHO is about 3-5 times faster than that of the HL by using the present simulation framework.

2.3 Fluid structure interaction

The fluid domain and the structure domain of a partitioned approach of FSI solver are coupled by kinematic and dynamic conditions at the interface of the two domains. The displacement of the fluid structure interface has to follow the kinematic condition as [1]:

$$\boldsymbol{d}_s = \boldsymbol{d}_f \tag{2.17}$$

where $\boldsymbol{d_s}$ and $\boldsymbol{d_f}$ represent the displacement at the fluid structure interface in the structure and fluid domains, respectively. The kinematic condition indicated that the displacement of the fluid structure interface has to be consistent between the two domains. When the displacement of the interface has been determined by the structural solver, it is applied to the fluid domain as a Dirichlet boundary condition.

The fluid forces or tractions acting on the fluid structure interface have to follow the dynamic condition as [11, 1]:

$$\sigma_s \cdot \boldsymbol{n} = \boldsymbol{t_f} \tag{2.18}$$

where $\boldsymbol{t_f}$ is the traction at the fluid structure interface, which is calculated as:

$$\boldsymbol{t_f} = \sigma_f \cdot \boldsymbol{n} \tag{2.19}$$

The stress tensor at the interface σ_f, which is calculated from the fluid domain with an incompressible Newtonian fluid is expressed as:

$$\sigma_f = -p\boldsymbol{I} + \tau \tag{2.20}$$

where p is the pressure forces and τ is the viscous component of the stress tensor that is calculated as:

$$\tau = \mu_f(\nabla \boldsymbol{U} + \nabla \boldsymbol{U}^T) \tag{2.21}$$

The dynamic condition indicated that the forces acting on the fluid structure interface has to be conserved between the two domains. When the forces at the interface has been determined by the fluid solver, it is applied to the structure domain as a Neumann boundary condition.

Loose coupling between fluid and structure domains is unstable. There are several coupling methods to help stabilise the simulation. Figure 2.1 summarises the coupling methods for partitioned FSI simulations. The Robin Boundary Condition and artificial compressibility require information on the discretisation or Jacobian of each domain and are not suitable for black-box solvers. The Reduced Order Modelling method is easy to implement and does not require sub-iterations. Jacobi-Like Coupling is stable for compressible solvers and unstable for incompressible solvers. For the fixed-point Gauss-Seidel iteration method, the displacement of the structure at the $(k+1)$th iteration, $\boldsymbol{d}_{k+1}$ could be expressed as:

$$\boldsymbol{d}_{k+1} = \boldsymbol{d}_k + \omega_k R_k \tag{2.22}$$

where ω_k is the under relaxation factor at the kth iteration and the residual of the FSI coupling at the kth iteration, R_k, is determined as:

$$R_k = \boldsymbol{F_s} \circ \boldsymbol{F_f}(\boldsymbol{d}_k) - \boldsymbol{d}_k \tag{2.23}$$

where the $\boldsymbol{F_s}$ and $\boldsymbol{F_f}$ are the interface operators for structure and fluid, respectively.

For a Fixed Relaxation method, the under relaxation factor can be expressed as:

$$\omega_k = constant \tag{2.24}$$

while for the Aitken's δ^2 method, the under relaxation factor is calculated as:

$$\omega_k = -\omega_{k-1} \frac{(R_{k-1})^T (R_k - R_{k-1})}{||R_k - R_{k-1}||^2} \tag{2.25}$$

A constraint can be applied to the Aitken's method to make it stable as:

$$\omega_k = sgn(\omega_k) min(|\omega_k|, \omega_{max}) \tag{2.26}$$

where ω_{max} is the maximum value of the under relaxation factors between the 1st and the kth iterations. The Fixed Relaxation method is easy to implement, requires less computational resources, but has a slow convergence speed. The Aitken's δ^2 method requires more computational resources than the Fixed Relaxation method, but has a quick convergence speed [11, 5].

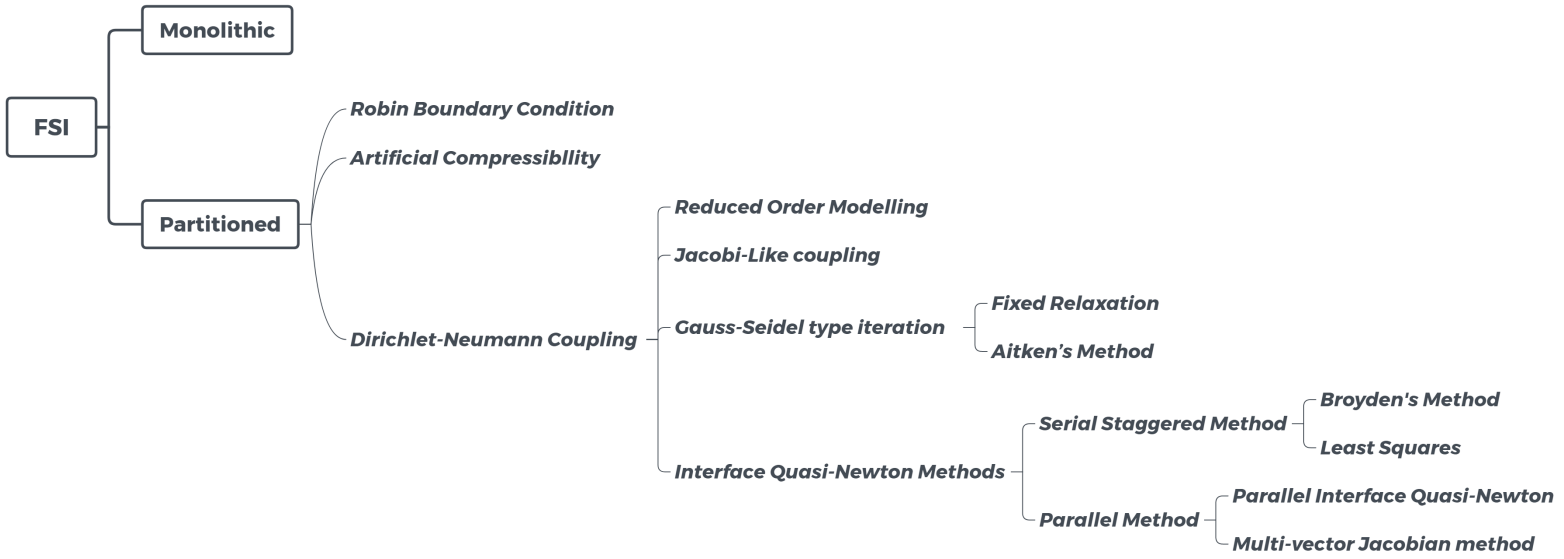

Figure 2.1: Summary on coupling method for FSI simulations.

The Interface Quasi-Newton Method provides a quick convergence speed and stability for strong coupling cases, but it is quite challenging to implement and requires certain amounts of computational resources.

Apart from the loose coupling, the present framework also implemented both the Fixed Relaxation and the Aitken's δ^2 methods with FSI sub-iterations implemented in both CFD and CSM solvers, as shown in Figure 2.2.

Figure 2.2 shows the flow chart of the present framework. The left-hand side is the CFD solver for the fluid domain and the right-hand side is the CSM solver for the structure domain. In the time step of $t = t + \delta t$ and sub-iteration $iter + 1$, the fluid domain solves the flow field giving us fluid forces at each cell of the fluid structure interface with the structural domain through the MUI library. The displacements at each cell of the interface are determined by the MUI coupling utility based on the fetched value from the structural domain. The calculated displacements of each cell at the interface are then applied to the fluid domain as a Dirichlet boundary condition. The structural domain fetch fluid forces and apply them as a Neumann boundary condition on the structure. It further calculated the deformation of the structure and push to the fluid solver. The stress of the structure will then be updated. Both fluid and structure domains are moved to the next sub-iteration after the completion of the above actions. Several sub-iterations are needed within each time step until a convergence is reached, i.e. the R_k is small enough to be below the criteria.

The Radial Based Function (RBF) that is implemented in the MUI library is used to ensure the forces at the interface are conserved between the two domains.

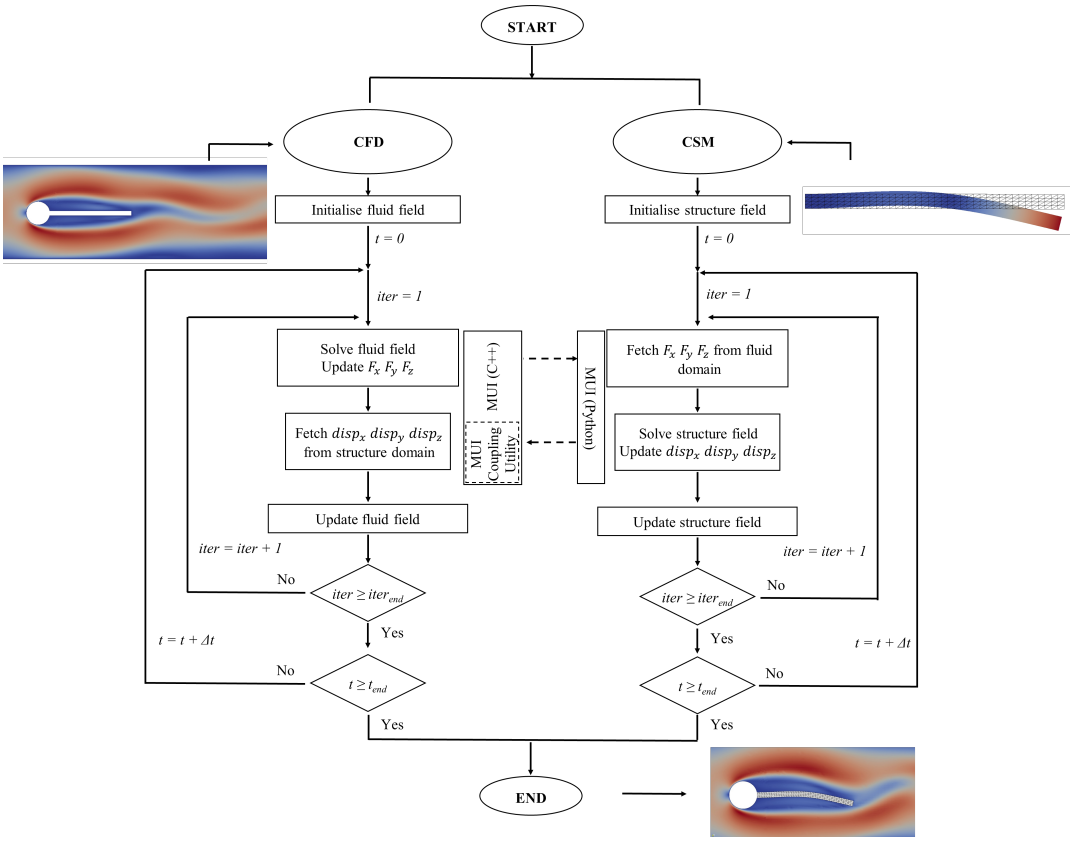

Figure 2.2: Flow chart of the developped FSI simulation framework.

Chapter 3

Validation of Framework

Six validation cases have been simulated and compared with published results for the developed MUI coupling utility, in-house solvers and the whole FSI framework.

3.1 1D Heat Transfer

The 1D heat transfer case has been calculated to validate the developed MUI coupling utility. Results and convergence speed of three coupling algorithms, i.e. Loose, Fixed Relaxation and Aitken, are compared. The simulation area is discretised into 10 nodes and split into 2 domains, as shown in 3.1. The left domain extends from node 0 to node 6, and right domain extends form node 4 to node 10. The overlapping zone is between node 4 and node 6 for the data sharing between the two domains. A heat source with $1^{\circ}C$ is applied to the node 0 and a heat sink with $0^{\circ}C$ is applied to the node 10. The 1D heat equation is applied to each node, which reads:

$$\frac{\partial T}{\partial i} = \kappa \frac{\partial^2 T}{\partial x^2} \tag{3.1}$$

where T is the temperature, i is the number of iterations, κ is the thermal conductivity that equals 0.515 for the present calculation and x is the coordinate of the node. The temperature is expected to reach the final state with a linear distribution along the 11 nodes. At each iteration, the temperature at node 6 is calculated by the right-hand side domain and sent to the left-hand side domain as the boundary condition, while the temperature at node 4 is determined by the left-hand side domain and sent to the right-hand side domain.

Figure 3.2 shows the calculation results at different iterations. Figure 3.2 (a) shows the initial state at the 1st iteration. As shown in Figure 3.2 (b), results from Aitken's method are closer to the final state than those from the Fixed Relaxation method, while the results from the Loose coupling started unphysical oscillation at the 51st iteration. At the 1000th iteration, as in Figure 3.2 (c), results from both

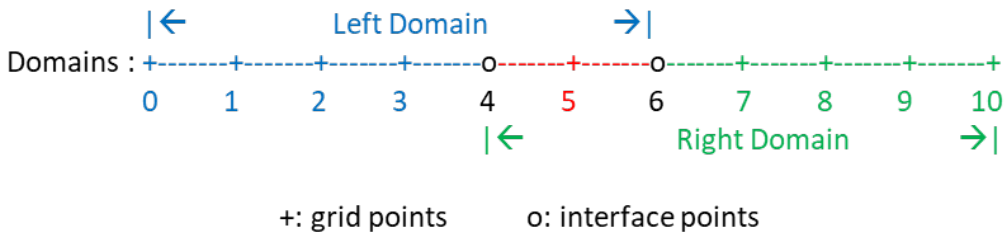

Figure 3.1: Schematic plot for the 1D heat transfer case.

Aitken's and Fixed Relaxation methods are reached to the final state, but the results from loose coupling are diverged.

Table 3.1 shows the number of iterations to the final state for different methods. It shows that the Aitken's method has the quickest convergence speed, while the coupled simulation is diverged by using Loose coupling.

Table 3.1: Iterations to Final State for different coupling method for the 1D heat transfer case.

Fixed Relaxation	**Aitken**	**Loose**
592	233	∞

3.2 Beam with Tip Load

In order to validate the in-house structure solver, an elastic beam with a tip load is simulated. A cantilever beam that with a clamped end and a free end has a density of $2600 kg/m^3$, Young's Modulus of 1.7×10^7 and Poission's Ratio of 0.3. The dimension of the cantilever beam is shown in Figure 3.3. An external force is applied to the free end towards the negative y-axis direction. The value of the force linearly increases to $500N$ from $0s$ to $7s$. After $7s$, the value of the force is equal to zero.

Figure 3.4 shows the contour plot of the shear stress. It is clear that the contour of the shear stress of the present simulation is qualitatively comparable with that of Slone et al. [9].

Figure 3.5 shows the instantaneous tip displacement of the beam. The difference between the present simulation and that of Slone et al. [9] is less than 1%.

3.3 2D Flow Pass Rigid Plate Behind a Rigid Cylinder

The benchmark case of a circular cylinder with a rigid plate in a 2D flow is simulated to validate the in-house `pimpleFSIFoam`. As shown in Figure 3.6, the 2D domain has a length of $2.5m$ and width of $0.41m$ with the original point located in the bottom left corner. The centre of the circular cylinder is located at $(0.2, 0.2)$,

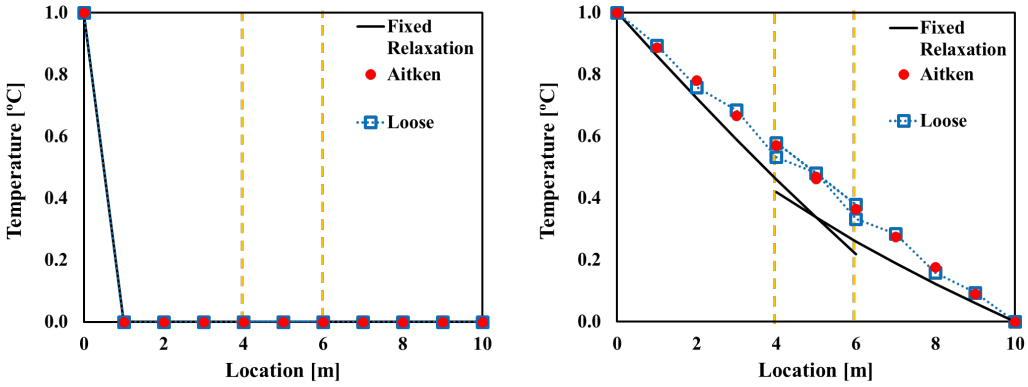

(a) The 1st iteration.

(b) The 51st iteration.

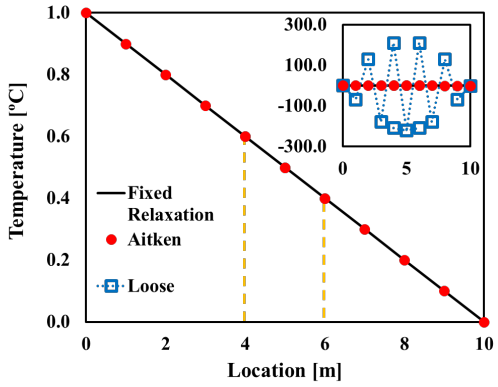

(c) The 1000th iteration.

Figure 3.2: Results of 1D Heat Transfer at different iteration. The area confined by the vertical dashed lines represents the overlapped zone

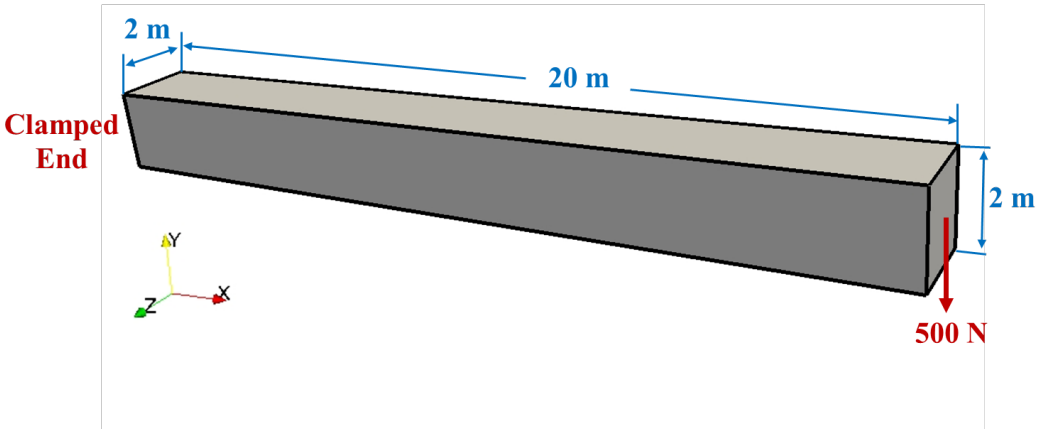

Figure 3.3: Schematic plot of the beam with tip load case.

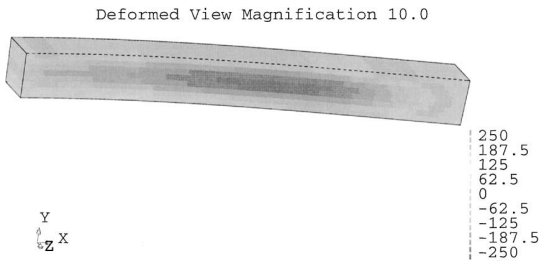

(a) Slone et al. [9].

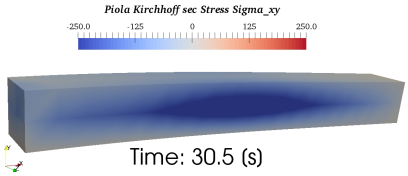

(b) Present simulation.

Figure 3.4: Stress contour of the beam with tip load case.

with a radius of $0.05m$. The rigid plate with a length of $0.35m$ and width of $0.02m$ is attached downstream of the cylinder. A parabolic x-axis velocity is applied to the left domain boundary with a peak velocity of $2m/s$. The density of the fluid is $1 \times 10^3 kg/m^3$. The kinematic viscosity is $1 \times 10^{-3} m^2/s$. The Reynold's number is calculated based on the maximum velocity that gives the value of 200.

Figure 3.7 shows the velocity contour. It is qualitatively comparable between the present simulation and the results from Slyngstad [1].

The lift and drag forces of the cylinder and the plate are compared with that from Turek and Hron [8] and presented in the Figure 3.8 and the Table 3.2. It proves the accuracy of the in-house `pimpleFSIFoam` solver.

Table 3.2: Forces of the Cylinder and Plate of the 2D Flow Pass Rigid Plate Behind a Rigid Cylinder Case.

	Drag [N]	**Lift [N]**
Present Simulation	442.40±5.88	-13.30±446.87
Turek and Hron [8]	439.95±5.62	-11.89±437.81
Error %	0.56%±4.69%	11.87%±2.07%

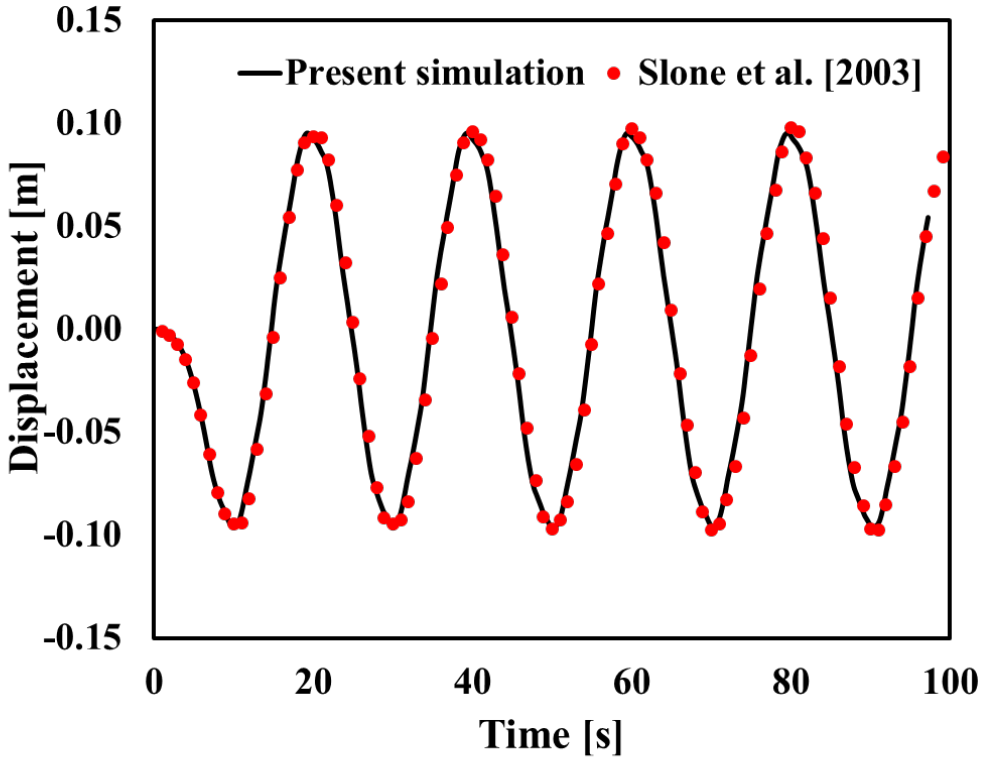

Figure 3.5: Displacement over time of the beam with tip load case.

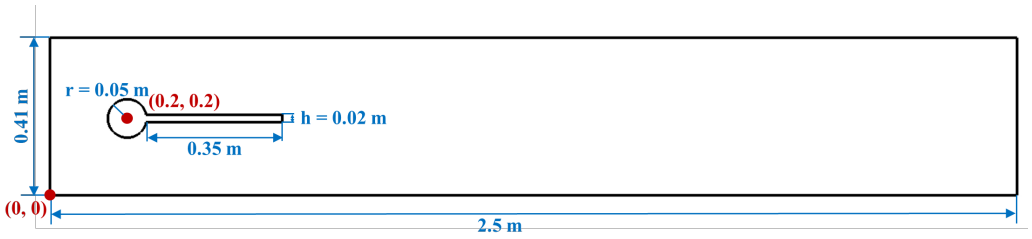

Figure 3.6: Schematic plot of the 2D flow pass rigid plate behind a rigid cylinder case.

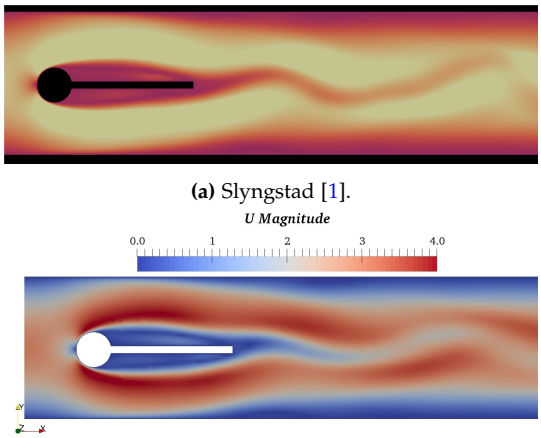

(a) Slyngstad [1].

(b) Present simulation.

Figure 3.7: Velocity contour of the 2D flow pass rigid plate behind a rigid cylinder case.

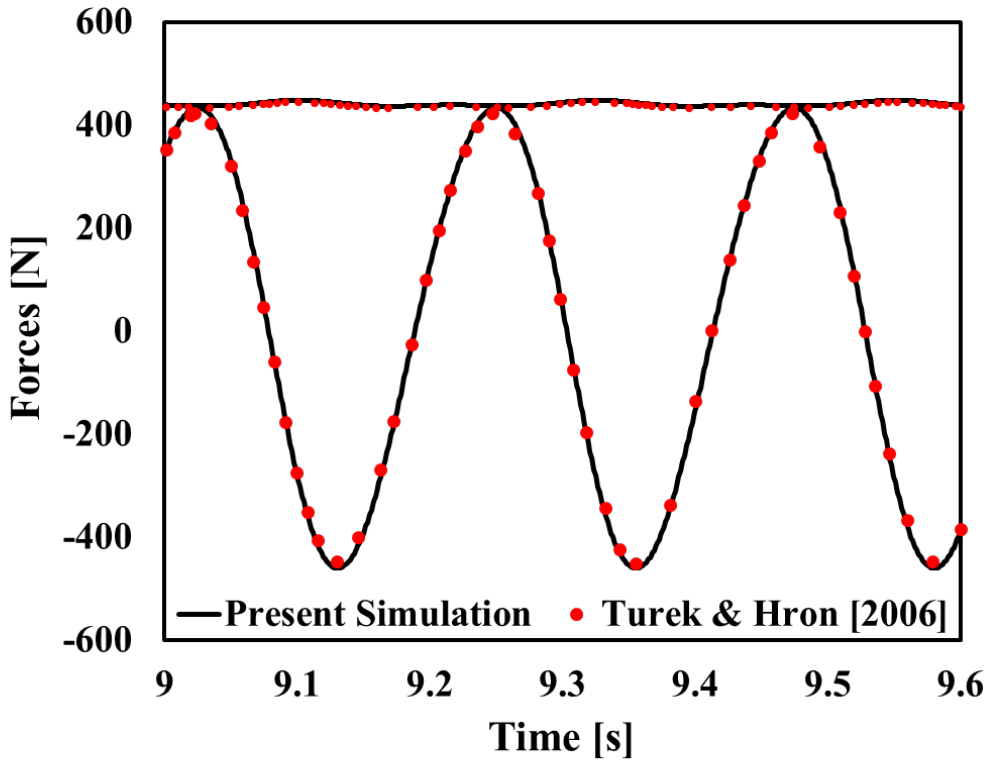

Figure 3.8: Forces over time of the 2D flow pass rigid plate behind a rigid cylinder case.

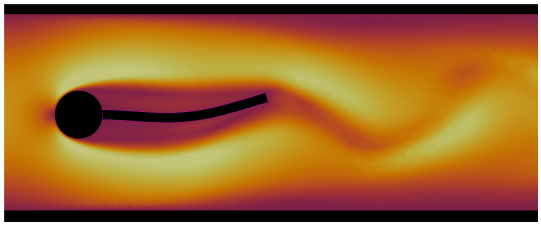

(a) Slyngstad [1].

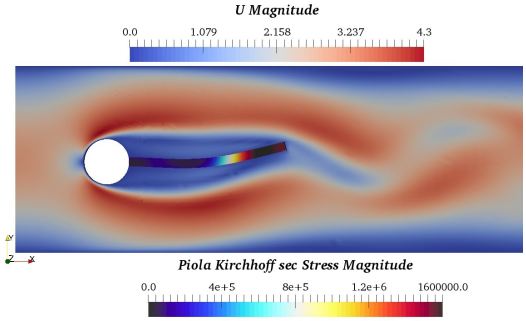

(b) Present simulation.

Figure 3.9: Velocity contour of the 2D flow pass elastic plate behind a rigid cylinder.

3.4 2D Flow Pass Elastic Plate Behind a Rigid Cylinder

After the validations of both the in-house structure solver and the in-house `pimpleFSIFoam` fluid solver, the entire FSI framework is validated by three benchmark cases. The first benchmark case is the circular cylinder with a flexible plate in a 2D flow. It has the same geometry and fluid condition as the CFD validation case (as discussed in Section 3.3). In the present case, the plate is flexible and has a density of $1 \times 10^3 kg/m^3$. The Poission's Ratio of the plate is 0.4 and Young's modulus is $5.6 \times 10^6 Pa$.

The velocity contour and the displacement of the plate are qualitatively comparable with Slyngstad [1], as shown in Figure 3.9. Moreover, the stress contour of the plate from the structure domain has also been presented.

The displacements of the tip of the flexible plate are quantitatively compared with Tukovic et al. [11] as shown in Figure 3.10. The difference between the tip displacement along the y-axis direction from the present simulation and that from Tukovic et al. [11] is less than 5%.

3.5 3D Parabolic Flow Over a Firmer Elastic Beam

The present FSI framework is also validated with a 3D benchmark case, which is a parabolic velocity past a flexible beam. The dimension of the simulation domain is shown in Figure 3.11. The density of the fluid is the same as the density of

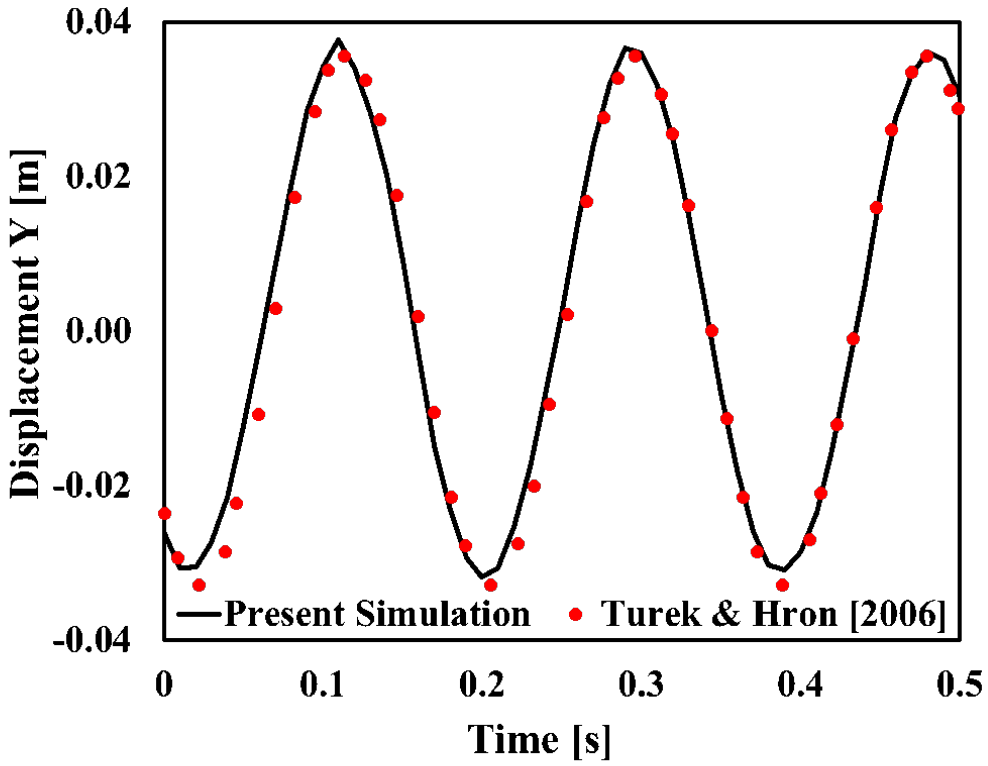

Figure 3.10: Displacement over time of the 2D flow pass elastic plate behind a rigid cylinder.

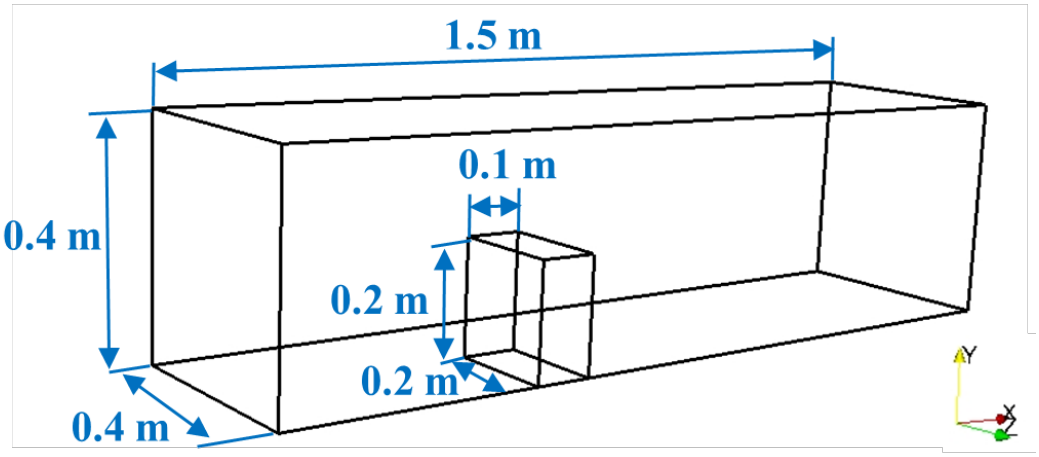

Figure 3.11: Schematic plot of the 3D parabolic flow over a firmer elastic beam.

the flexible beam, which is $1000kg/m^3$. The kinematic viscosity of the fluid is $0.001m^2/s$. The peak velocity is $0.2m/s$. The flexible beam has a Young's mudulus of $1.4 \times 10^6 Pa$ and a Poission's ratio of 0.4.

Table 3.3: Displacement of the Firmer Elastic Beam.

	Displacement X [m]	**Displacement Y [m]**
Present Simulation	5.95×10^-5	2.36×10^-5
Tukovic et al. [11]	5.93×10^-5	2.40×10^-5
Richter [10]	5.95×10^-5	-
Error %	+0.34%	-1.67%

The instantaneous x-axis displacement at the point $(0.45, 0.15, 0.15)$ is shown in Figure 3.12. The x-axis and y-axis displacements at the point $(0.45, 0.15, 0.15)$ in the steady state are listed in Table 3.3 and compared with Richter [10] and Tukovic et al. [11]. The present simulation has the same x-axis displacement with that of Richter [10]. The difference between the displacements from the present simulation and from Tukovic et al. [11] is less than 2%.

3.6 3D Parabolic Flow Over a Softer Elastic Beam

In order to demonstrate the ability of the present FSI framework to handle challenging FSI cases, the 3D benchmark case as discussed in Section 3.5 has been simulated again with a softer beam. The Young's Modulus of the beam is $1 \times 10^4 Pa$ and the peak velocity is $0.3m/s$. Other fluid/structure parameters remained the same as the 3D benchmark case in Section 3.5.

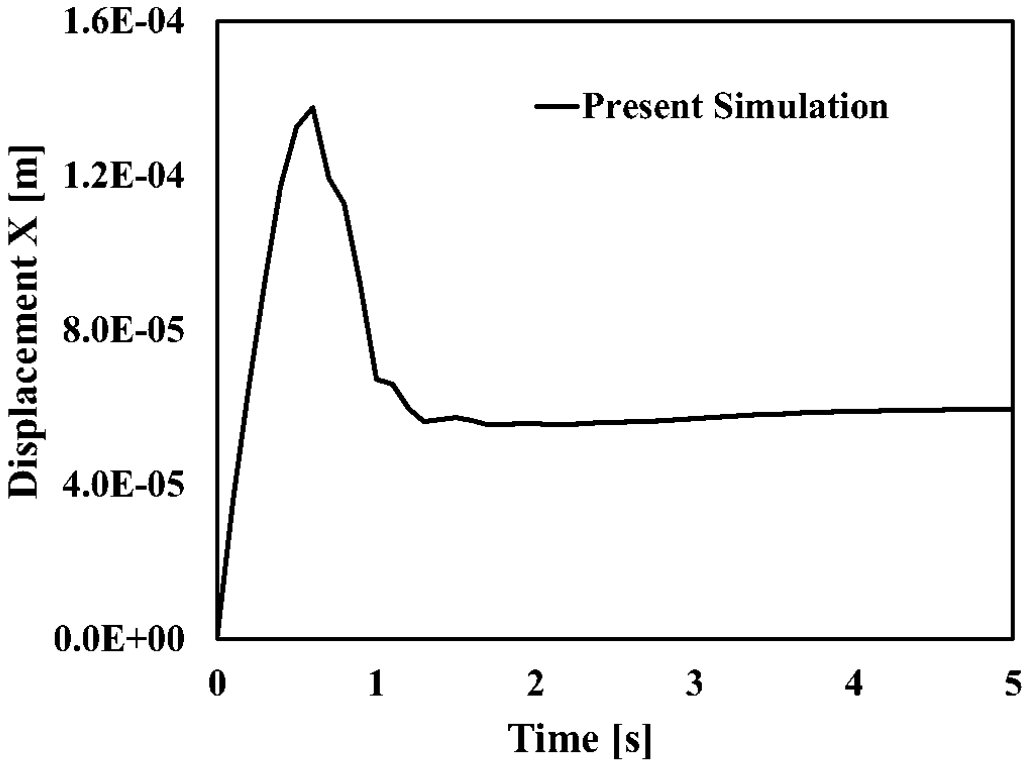

Figure 3.12: Displacement over time of the 3D parabolic flow over a firmer elastic beam.

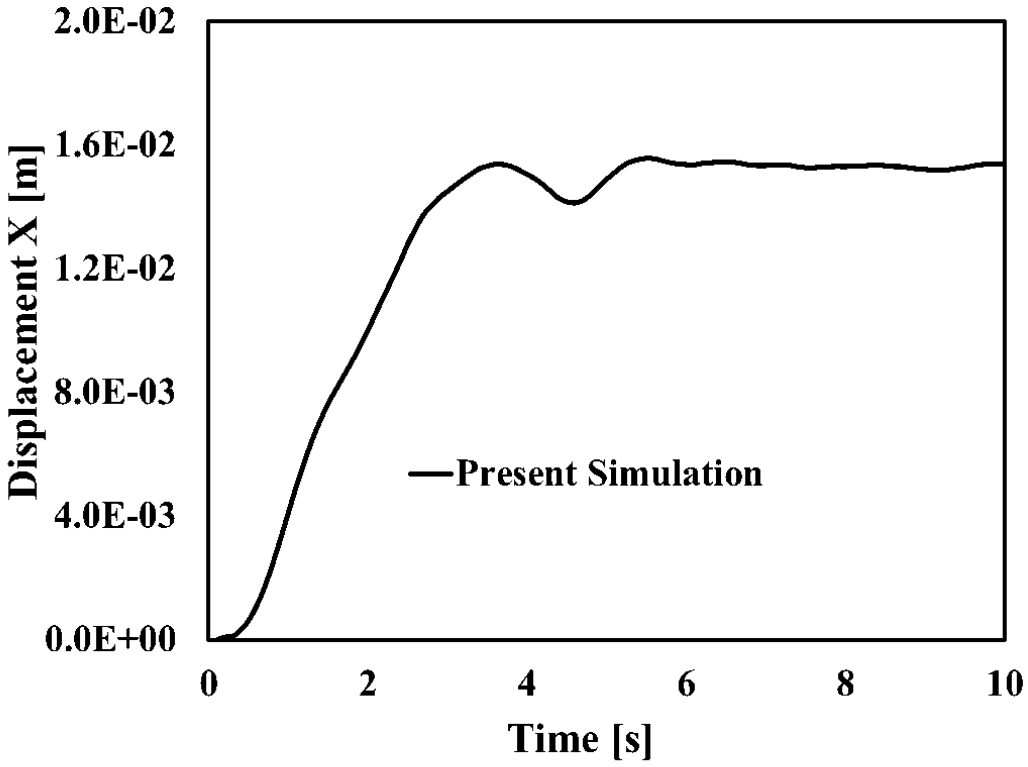

Figure 3.13: Displacement over time of the 3D parabolic flow over a softer elastic beam.

The instantaneous displacement along x-axis direction of the flexible beam at the point $(0.45, 0.15, 0.15)$ is presented in Figure 3.13. The velocity contour of the fluid domain and the displacement contour of the structure domain are qualitatively comparable with that of Tukovic et al. [11], as shown in Figure 3.14. The x-axis and y-axis displacements at the point $(0.45, 0.15, 0.15)$ in the steady state are listed in the Table 3.4 and compared with Tukovic et al. [11]. The difference between the present simulation and that of Tukovic et al. [11] is up to 4.6%, which shows a good accuracy of the present developed framework on simulating challenging FSi problems.

Table 3.4: Displacement of the Softer Elastic Beam.

	Displacement X [m]	**Displacement Y [m]**
Present Simulation	$1.52 \times 10^{-}2$	$4.77 \times 10^{-}3$
Tukovic et al. [11]	$1.46 \times 10^{-}2$	$5.00 \times 10^{-}3$
Error %	+4.11%	-4.60%

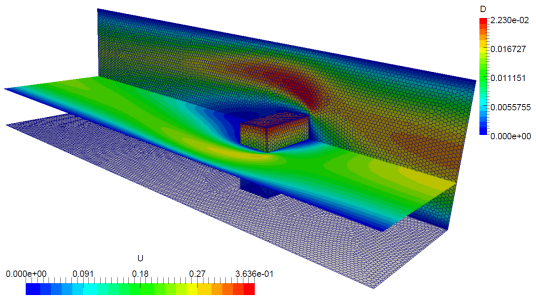

(a) Tukovic et al. [11].

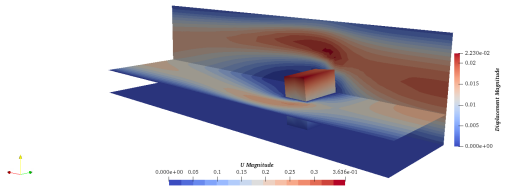

(b) Present simulation.

Figure 3.14: Velocity contour of the 3D parabolic flow over a softer elastic beam.

Chapter 4

Scalability Test of Framework

Scalability tests have been realised for the present FSI simulation framework. The fully coupled 3D FSI benchmark case that is discussed in 3.5 is chosen. The scalability tests are carried out by varying the number of CPU cores of the fluid and structure solvers, respectively: A fixed CPU core of 100 for the structure domain (in-house structure solver) and varying the CPU cores up to 1000 of the fluid domain (in-house pimpleFSIFoam) to test the scaling performance of the pimpleFSIFoam; and a fixed CPU core of 500 for the fluid domain and varying the CPU cores up to 1000 of the structure domain to test the scaling performance of the in-house structure solver. The total number of the hexahedral cells in the fluid domain is $83M$ and the number of degrees of freedom (DoF) in the structure domain is $2.5M$.

As shown in Figure 4.1, the in-house pimpleFSIFoam has a good performance on scalability with a parallel efficiency of about 68% for 1000 CPU cores in the fluid domain, while the parallel efficiency of the in-house structure solver is only 40% for 1000 CPU cores in the structure domain. The reason for the less ideal performance of the in-house structure solver might be that the algorithms of the calculation of the stress in each time step do not have good scalability. In addition, the number of DoFs may not be large enough causing the communications between CPU cores to occupy a large proportion of the computational resources and simulation time.

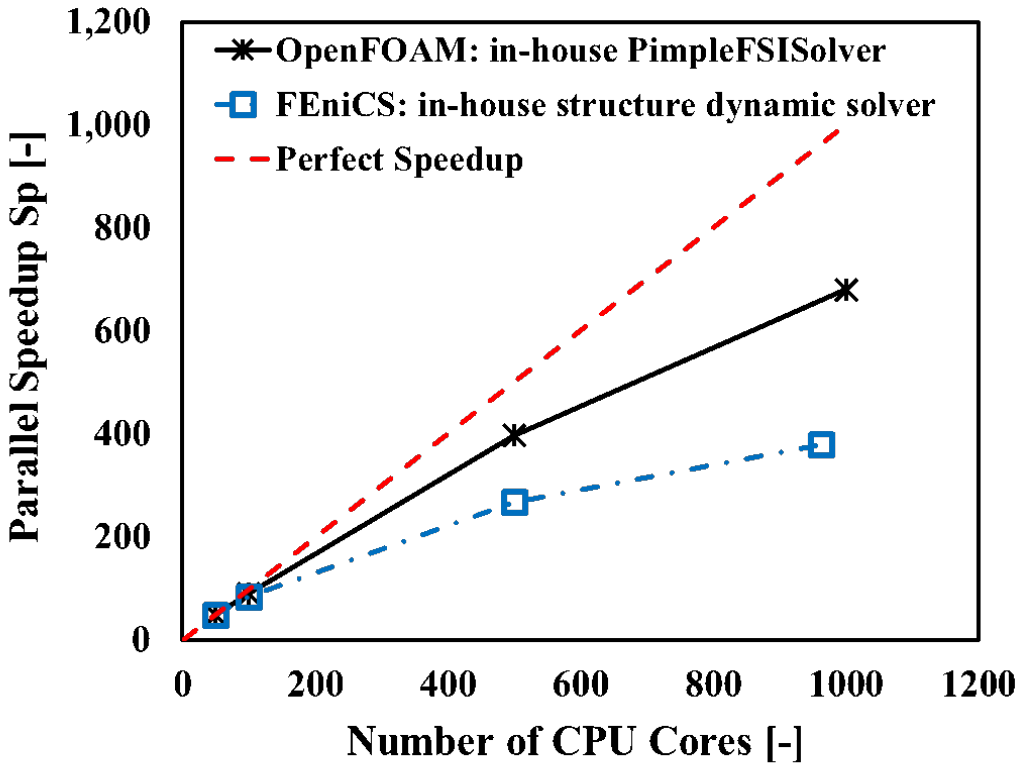

Figure 4.1: Scalability Test Result on the FSI Simulation Framework.

Chapter 5

Hydrofoil Case

In this chapter, the vortex-induced vibration of the trailing edge of a hydrofoil is simulated and compared with the experimental results from Ausoni [6].

5.1 Physical properties

The NACA 0009 hydrofoil is immersed into a uniform incoming flow as shown in Figure 5.1 with the Angle of Attack (AoA) equals zero. The x-axis velocity of the incoming flow is C_ref, while the y and z-axis velocity remain zero. The density of the fluid is $998kg/m^3$ and kinetic viscosity is $1 \times 10^{-6}m^2/s$. The hydrofoil has a chord length, L, of $1000mm$ and span length, B, of $150mm$. The hydrofoil has a tripped trailing edge with a height, h, of $3.22mm$. The hydrofoil has a perfect embedding at $z = 0$ plane and has a pivot embedding at the centre of the $z = 0.15$ plane. The density of the hydrofoil is $7800kg/m^3$. The Young's modulus and Poission's ratio of the hydrofoil are 2.1×10^11Pa and 0.3.

The Reynolds's number, Re_h is defined as:

$$Re_h = \frac{\rho h C_{ref}}{\mu} \tag{5.1}$$

According to the experiment, the lock-in regime for the tripped hydrofoil is in the region of $4.80 \times 10^4 \leq Re_h \leq 5.35 \times 10^4$.

5.2 Simulation setup

The fluid domain extends $0.5L$ away from the leading edge of the hydrofoil towards the upstream, $7L$ away from the leading edge towards the downstream and $0.7L$ away towards both the maximum and minimum y-axis domain boundaries.

Both 2D (i.e. employed one cell along the span wise direction in the fluid domain) and 3D (i.e. employed 100 cells along the span wise direction in the

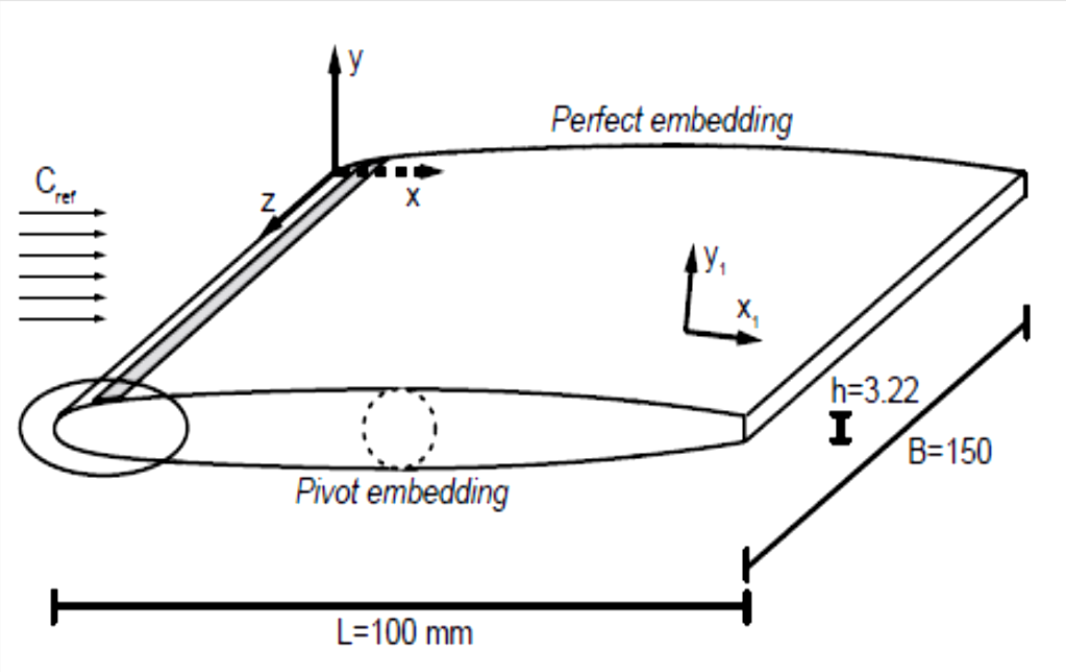

Figure 5.1: Schematic plot of the Hydrofoil case from Ausoni [6].

fluid domain) fluid meshes are used for the fully coupled FSI simulations. The total number of the fluid cells employed in the present simulation are $0.145M$ and $14.5M$ for 2D and 3D meshes, respectively. A 3D tetrahedral mesh is employed for the structure domain.

A grid sensitivity test for the structure domain is carried out, which shows the difference between the results calculated by the fine grid ($22767DoFs$) and that by the medium grid ($6699DoFs$) is much less than the coarse grid ($3257DoFs$). Therefore, the medium grid with $6699DoFs$ is employed for the hydrofoil simulation.

The topology of the fluid and structure grids employed in the present simulation is presented in Figure 5.2.

Four cases have been simulated by using the 2D fluid mesh, which are 3.86×10^4 (before the lock-in regime), 4.83×10^4 (the beginning of the lock-in regime), 5.31×10^4 (the end of the lock-in regime) and 7.08×10^4 (the lock-off regime). Three cases have been simulated by using the 3D fluid mesh, which are 3.86×10^4 (before the lock-in regime), 4.83×10^4 (the beginning of the lock-in regime) and 6.44×10^4 (the lock-off regime).

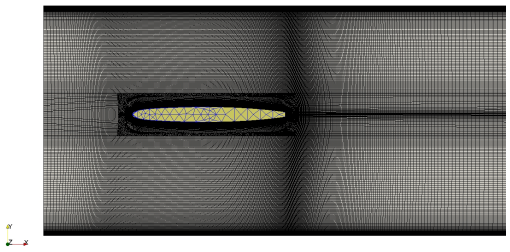

(a) Zoomed out view of the domain.

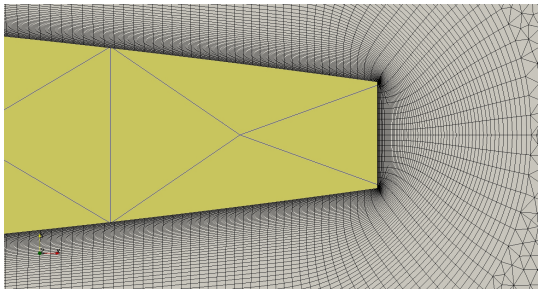

(b) Zoomed in view at the trailing edge of the hydrofoil.

Figure 5.2: Mesh for both the fluid and structure domains of the hydrofoil case

5.3 Results on frequency and amplitude of hydrofoil vibration

The frequency ratio is defined as the frequency of the displacement velocity at $(0.08, 0.003788, 0.1125)$, (f_s), to the natural frequency of the hydrofoil, (f_n). The results on the frequency ratio in different Re_h for both 2D and 3D simulations are presented and compared with Ausoni [6] in Figure 5.3.

Generally, both 2D and 3D results are comparable with the experimental results with a maximum difference of about 8%.

The results on standard deviation of the displacement velocity at $(0.08, 0.003788, 0.1125)$ for different Re_h are shown and compared with the experiential results in Figure 5.4. The results from the 2D simulation are over predicted compared to the 3D simulations. This is because the 2D simulation doesn't have sufficient resolution along the span wise direction, so that the turbulence-induced fluid forces reduction is under predicted.

5.4 Instantaneous results on vibration velocity and spectra

The displacement velocity of the hydrofoil at $(0.08, 0.003788, 0.1125)$ for three Reynold's numbers are shown in Figure 5.5. The instantaneous velocity at the lock-in regime

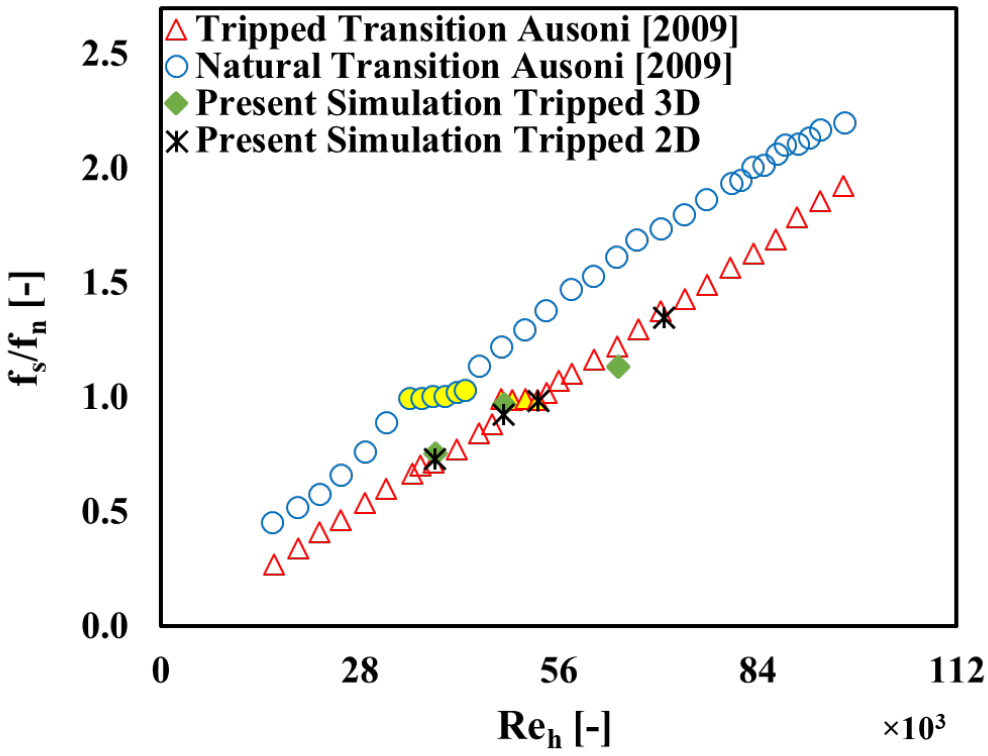

Figure 5.3: Frequency ratio over Reynold's number of the hydrofoil case compared with Ausoni [6].

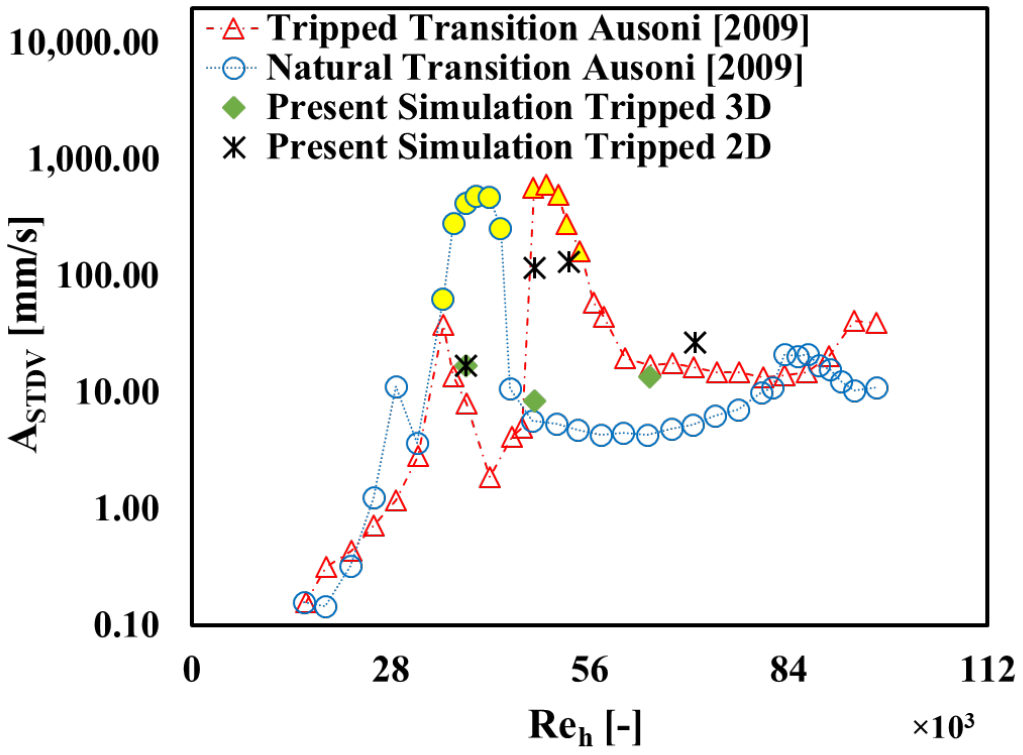

Figure 5.4: Standard deviation of vibration amplitude over Reynold's number of the hydrofoil case compared with Ausoni [6].

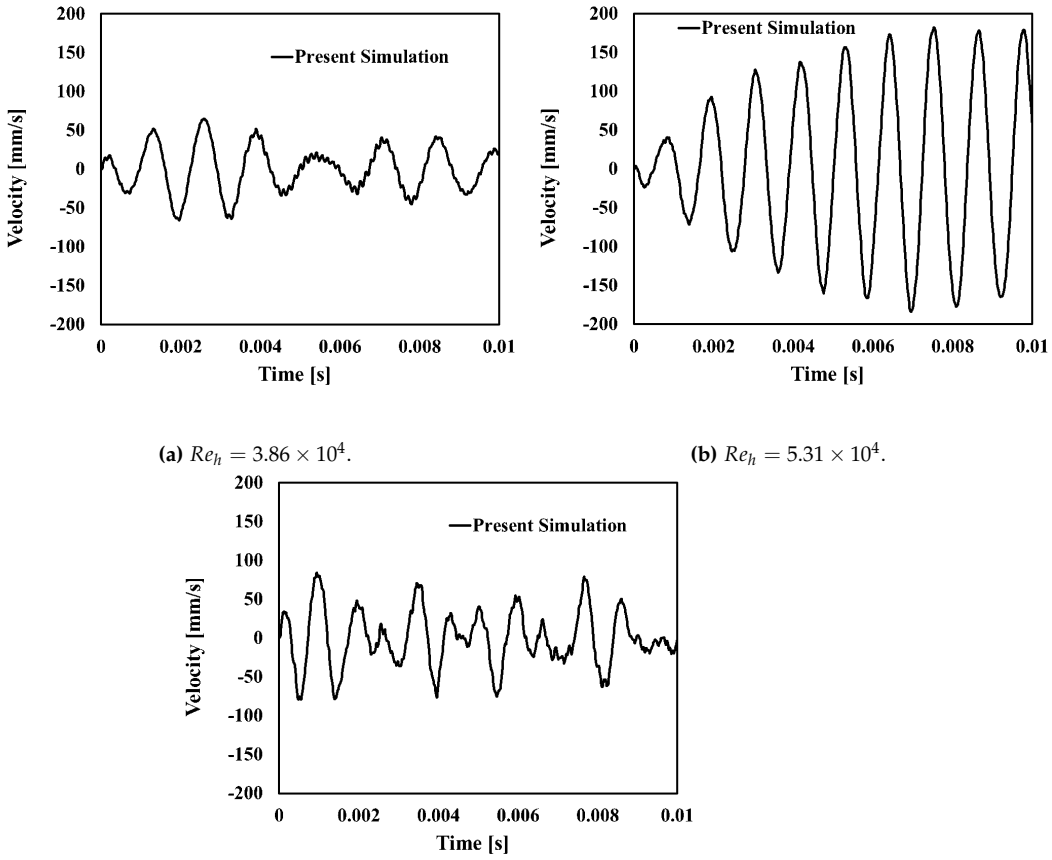

(a) $Re_h = 3.86 \times 10^4$.

(b) $Re_h = 5.31 \times 10^4$.

(c) $Re_h = 7.08 \times 10^4$.

Figure 5.5: Instantaneous vibration velocity of the hydrofoil case

(Figure 5.5 (b)) has significant features that can easily be distinguished from that of other regimes: large amplitude and regular spikes. These features are also shown in the velocity spectra plot in Figure 5.6. The lock-in regime velocity has one dominant frequency with a large power spectral density, while the velocity in other regimes has two or more dominant frequencies with relatively small power spectral densities.

5.5 Contours on fluid and structure domains

The pressure and velocity contours of the fluid domain at the time instants that the hydrofoil reaches its maximum displacement are shown in Figure 5.7 and Figure 5.8, respectively. The vortices in the wake of the hydrofoil are clearly seen for different Re_h.

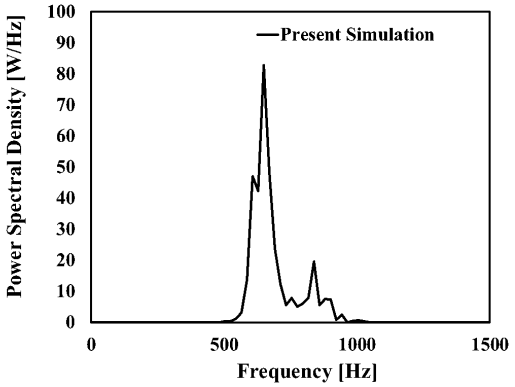

(a) $Re_h = 3.86 \times 10^4$.

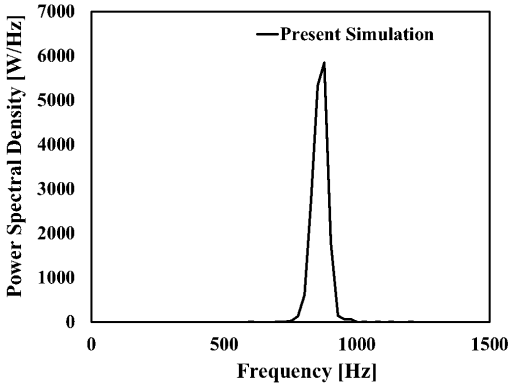

(b) $Re_h = 5.31 \times 10^4$.

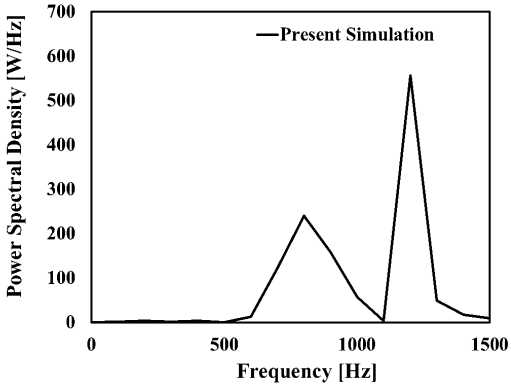

(c) $Re_h = 7.08 \times 10^4$.

Figure 5.6: Vibration spectra of the hydrofoil case

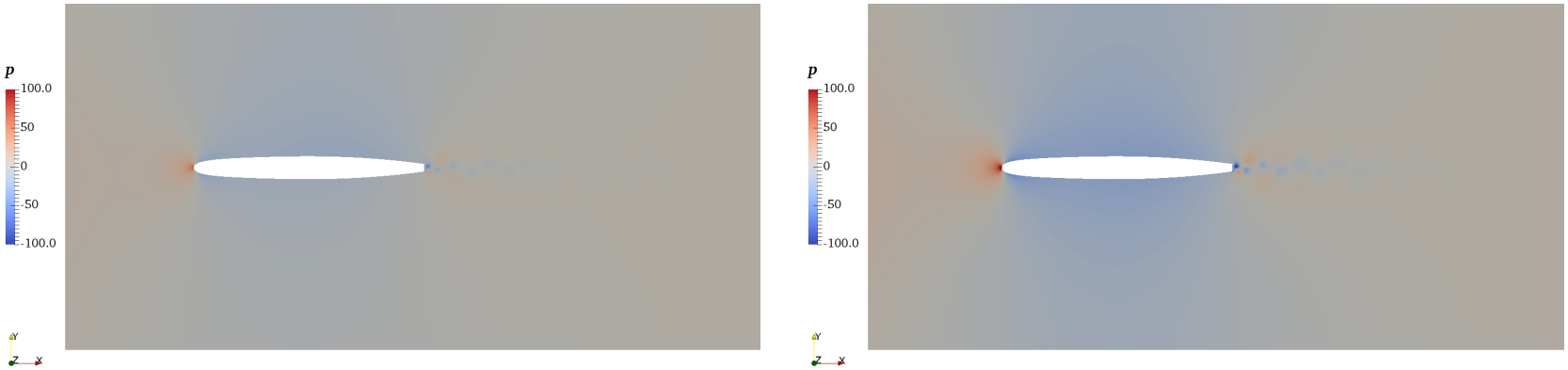

(a) $Re_h = 3.86 \times 10^4$ at $t = 0.0197$s.

(b) $Re_h = 5.31 \times 10^4$ at $t = 0.0203$s.

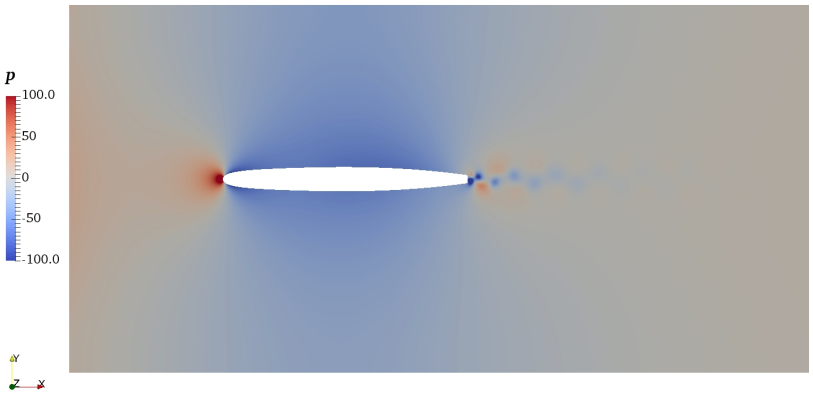

(c) $Re_h = 7.08 \times 10^4$ at $t = 0.0204$s.

Figure 5.7: Pressure contour of the hydrofoil case

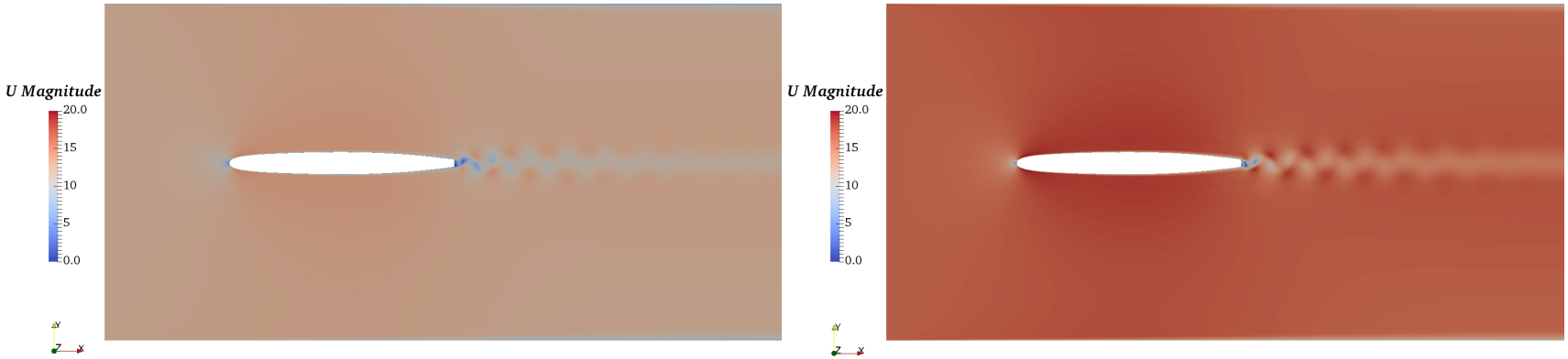

(a) $Re_h = 3.86 \times 10^4$ at $t = 0.0197$s.

(b) $Re_h = 5.31 \times 10^4$ at $t = 0.0203$s.

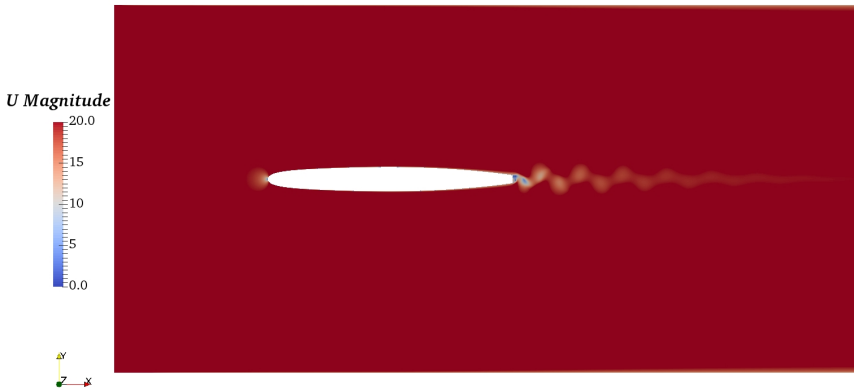

(c) $Re_h = 7.08 \times 10^4$ at $t = 0.0204$s.

Figure 5.8: Velocity contour of the hydrofoil case

The stress distribution of the hydrofoil at the time instants that the hydrofoil reaches its maximum displacement for different Re_h are shown in Figure 5.9. The hydrofoil subjected a large stress at midspan when it reached the largest displacement. Figure 5.10 shows the displacement of the hydrofoil with magnification of 1,000. It can be seen that the displacement is much larger in the lock-in regime than in the others.

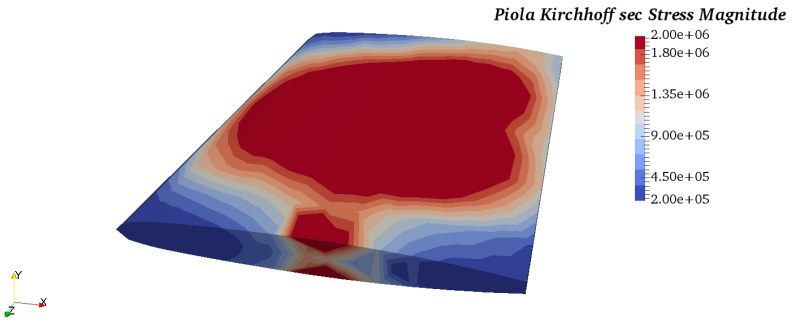

(a) $Re_h = 3.86 \times 10^4$ at $t = 0.0197$s.

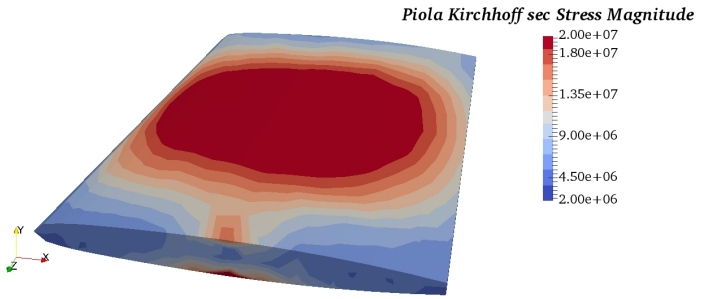

(b) $Re_h = 5.31 \times 10^4$ at $t = 0.0203$s.

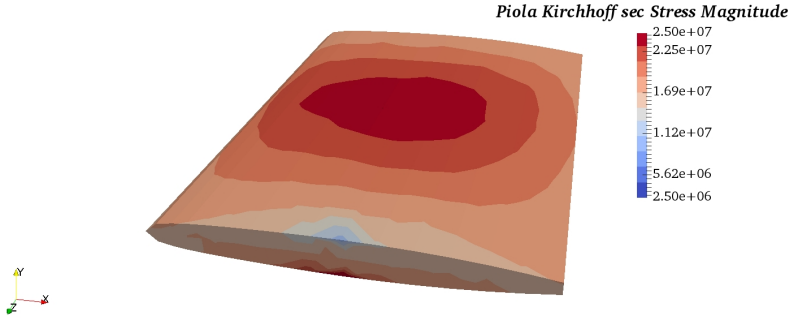

(c) $Re_h = 7.08 \times 10^4$ at $t = 0.0204$s.

Figure 5.9: Stress contour of the hydrofoil case

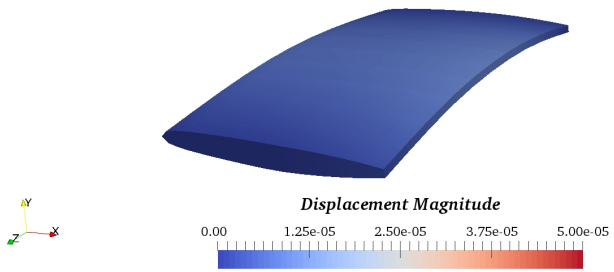

(a) $Re_h = 3.86 \times 10^4$ at $t = 0.0197$s.

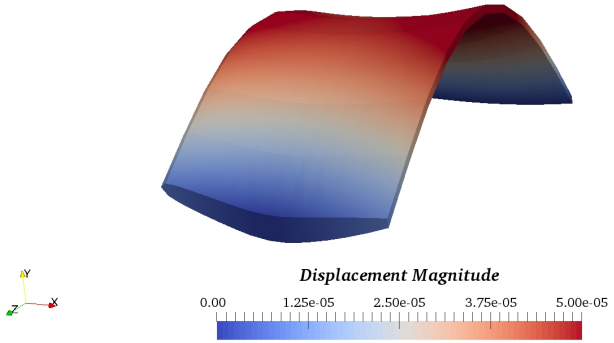

(b) $Re_h = 5.31 \times 10^4$ at $t = 0.0203$s.

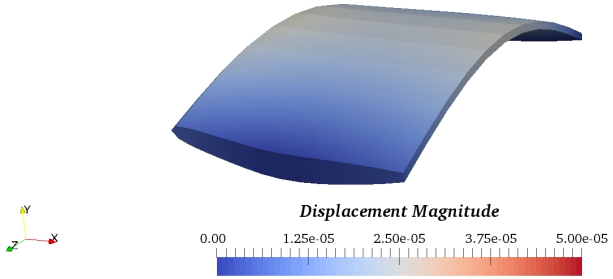

(c) $Re_h = 7.08 \times 10^4$ at $t = 0.0204$s.

Figure 5.10: Displacement contour of the hydrofoil case with magnification 1,000

Chapter 6

Conclusions and recommendations

We have developed an effective and robust method for fluid-structure interaction simulations by using a partitioned approach. The MUI coupling library is employed as the interface between fluid and structure domains. OpenFOAM and FEniCS are adopted as the CFD and CSM solvers, respectively. Two explicit/implicit coupling utilities, i.e. the Fixed Relaxation approach and the Aitken's δ^2 approach, for the FSI coupling have been implemented in the MUI library to achieve a tight and stable coupling. According to the verification test on the MUI coupling utilities, both Fixed Relaxation and the Aitken's δ^2 approaches are able to achieve stable coupling for challenging cases. However, the Aitken's δ^2 approach can save half of the computational resources to reach convergence compared with the Fixed Relaxation approach. Five validation cases have been conducted by using the newly developed Partitioned Multi-physical Simulation Framework (see Appendix A) and compared with published results, which show good accuracy of the present framework. A preliminary scalability test has been done for the developed framework. The results of vortex-shedding induced vibration of a hydrofoil have been conducted and presented. A comparison between the numerical simulation and the experimental data shows the capability of the present simulation framework to undertake challenging FSI simulations. The FSI framework is able to model FSI cases with both small and large structure deformations, but valid for small strains. A large structural deformation usually means the order of magnitude of the deformation is closed to that of the cord/span length of the structure. Since the mesh motion of the CFD solver is achieved by the Arbitrary Lagrangian-Eulerian (ALE) method, the mesh quality may reduce, which leads to unreliable results when the order of magnitude of the deformation is larger than that of the cord/span length of the structure. Further development of the FSI framework is ongoing. The scalability of the framework needs to be further enhanced to enable large simulations. More solvers will be involved in the framework to make it flexible and meet the needs of different simulation cases.

Bibliography

[1] Slyngstad A.S. "Verification and Validation of a Monolithic Fluid-Structure Interaction Solver in FEniCS. A comparison of mesh lifting operators". In: *Master's thesis* (2017).

[2] Bonaventura L. Erlicher S. and Bursi O. "The analysis of the Generalized-alpha method for non-linear dynamic problems". In: *Computational Mechanics* 28 (2002), pp. 83–104.

[3] Jasak H. "Dynamic Mesh Handling in OpenFOAM". In: *47th AIAA Aerospace Sciences Meeting Including The New Horizons Forum and Aerospace Exposition*. 2009, p. 341.

[4] Bleyer J. "Numerical Tours of Computational Mechanics with FEniCS". In: (2018).

[5] Scheufele K. "Robust Quasi-Newton methods for partitioned fluid-structure simulations". Master's thesis. 2015.

[6] Ausoni P. "Turbulent vortex shedding from a blunt trailing edge hydrofoil." In: *PhD thesis* (2009).

[7] Hron J. Acker J. Weichert F. Grunwald I. Roth C. Wagner M. Razzaq M. Turek S. and Romeike B. "Numerical simulation and benchmarking of fluid-structure interaction with application to hemodynamics". In: *In Fundamental Trends in Fluid-Structure Interaction* (2010), pp. 171–199.

[8] Turek S. and Hron J. "Proposal for numerical benchmarking of fluid-structure interaction between an elastic object and laminar incompressible flow". In: *Fluid-structure interaction*. 2006, pp. 371–385.

[9] Bailey C. Slone A.K. and Cross M. "Dynamic solid mechanics using finite volume methods". In: *Applied mathematical modelling* (2003), pp. 69–87.

[10] Richter T. "Goal-oriented error estimation for fluid–structure interaction problems". In: *Computer Methods in Applied Mechanics and Engineering* 223 (2012).

[11] Cardiff P. Jasak H. Tuković Ž. Karač A. and Ivanković A. "OpenFOAM finite volume solver for fluid-solid interaction". In: *Transactions of FAMENA*. 2018, pp. 1–31.

Appendix A

Partitioned Fluid-Structure Interaction Simulation Framework

Partitioned Fluid-Structure Interaction Framework is developed based on the MUI library and offers a platform where users can carry out multi-physical (mainly fluid-structure interaction) studies with High Performance Computers.

The framework uses partitioned approach to couple two or more physical domains together for a multi-physical simulation. It takes several advantages of the MUI library:

- Flexible of select solvers for each physical domain;
- Flexible of extend the number of physical domains;
- Good scalability on communications among physical domains for large simulations.
- Keep development of the coupled solvers decoupled. It allows for easier independent testing of each solver and avoid potential incompatibilities between two solvers (i.e if they both use a certain library X each one depends on a different version of it which are not compatible)
- Couple two solvers which have two different programming language interfaces(e.g C++ and Python).
- "Plug and play" strategy. One solver can be replaced by another incrementally and without the need of recompiling if the MUI interface is used as a common adaptor.
- Use two solvers which have two incompatible licenses exploiting the dual licensing of the MUI library (both solvers are never mixed source-wise or binary-wise).

This framework is under active development to involve more solvers as well as more physical domains. Such infrastructure will make it possible to simulate large multi-physical problems and simulate complicated multi-physical cases.